

Wet Extreme Mass Ratio Inspirals May Be More Common For Spaceborne Gravitational Wave Detection

Zhen Pan,^{1,*} Zhenwei Lyu,^{1,2} and Huan Yang^{1,2,†}

¹Perimeter Institute for Theoretical Physics, Waterloo, Ontario N2L 2Y5, Canada

²University of Guelph, Guelph, Ontario N1G 2W1, Canada

Extreme Mass Ratio Inspirals (EMRIs) can be classified as dry EMRIs and wet EMRIs based on their formation mechanisms. Dry (or the “loss-cone”) EMRIs, previously considered as the main EMRI sources for the Laser Interferometer Space Antenna, are primarily produced by multi-body scattering in the nuclear star cluster and gravitational capture. In this Letter, we highlight an alternative EMRI formation channel: (wet) EMRI formation assisted by the accretion flow around accreting galactic-center massive black holes (MBHs). In this channel, the accretion disk captures stellar-mass black holes that are initially moving on inclined orbits, and subsequently drives them to migrate towards the MBH - this process boosts the formation rate of EMRIs in such galaxies by orders of magnitude. Taking into account the fraction ($O(10^{-2} - 10^{-1})$) of active galactic nuclei where the MBHs are expected to be rapidly accreting, we forecast that wet EMRIs will contribute an important fraction of all EMRIs observed by spaceborne gravitational wave detectors and likely dominate for MBH hosts heavier than a few $10^5 M_\odot$.

Introduction. The primary astrophysical sources for space-based gravitational wave detectors, such as Laser Interferometer Space Antenna (LISA) [1] and TianQin [2], include massive black hole (MBH) binaries, extreme mass ratio inspirals (EMRIs), galactic binaries and stellar-mass black hole (sBH) binaries. Other systems, e.g. intermediate mass ratio inspirals [3, 4], extremely large mass ratio inspirals [5, 6] and cosmic strings [7], may also be detectable, *albeit* with larger uncertainties. Among these sources, EMRIs provide unique opportunities in testing the Kerr spacetime [8, 9], probing the galactic-center cluster distribution [10–12], understanding the astrophysical environmental effects [13–15], and inferring the growth history of MBHs [16–18]. Loud EMRIs can serve as dark standard sirens for measuring the Hubble constant H_0 and the dark energy equation of state [19].

EMRI formation mechanism can be classified into two main channels. In the “dry EMRI” channel, an EMRI may be produced after a sBH is gravitationally captured by a MBH, following the multi-body scatterings within the nuclear cluster [20–22]. There are two characteristic timescales [23, 24] in this process: the GW emission timescale t_{gw} on which the sBH orbit shrinks and the relaxation timescale t_J on which the orbital angular momentum of the sBH changes, due to scatterings by stars and other sBHs. If $t_{\text{gw}} > t_J$, the sBH will likely be randomly scattered either into or away from the MBH (sBHs scattered into the MBH are known as prompt infalls). If $t_{\text{gw}} < t_J$, the sBH orbit gradually spirals into the MBH to form an EMRI while random scatterings are negligible. The generic rate can be obtained by solving the Fokker-Planck equation or by N-body simulations [10–12], subject to assumptions on the initial distributions of stars and sBHs in the nuclear cluster. In addition to the generic rate per MBH, the EMRI rate density in the universe also depends on the mass function of MBHs, the fraction of MBHs living in stellar cusps and the relative abundance of sBHs in stellar clusters. Taking into account these astrophysical uncertainties, Babak et al. [21, 22] and Fan et al. [25] forecasted that there will be a few to thousands of detectable (dry) EMRIs per year by LISA

and TianQin, respectively. In a recent paper [26], Zwick et al. reanalyzed the GW emission timescales of inspiraling eccentric binaries and realized Post-Newtonian (PN) corrections to the commonly used Peters’ formula [27] are necessary. With PN corrections implemented, the dry EMRI rate decreases by approximately one order of magnitude.

Wet EMRIs come from MBHs in gas-rich environments, where the distributions of nearby stars and sBHs are significantly affected by the accretion flow. About 1% low-redshift ($z \lesssim 1$) galaxies and 1% – 10% high-redshift ($1 \lesssim z \lesssim 3$) galaxies are active [28, 29] and known as active galactic nuclei (AGNs), in which galactic MBHs are believed to be rapidly accreting gas in a disk configuration. In the presence of an accretion disk, the periodic motion of a sBH generally generates density waves which in turn affect the sBH’s motion by damping both the orbital inclination with respect to the disk plane and the orbital eccentricity, and driving the sBH’s migration in the radial direction [30–33]. As long as the sBH is captured onto the disk, the density waves together with other disk-sBH interactions, e.g., head wind [34], accelerate its inward migration until to the vicinity of the MBH where GW emissions become prevalent. In this Letter, we show that an accretion disk usually boosts the EMRI intrinsic rate per individual MBH by orders of magnitude compared with the loss-cone channel [35]. In particular, we suggest that (wet) EMRI formation in AGN disks is an important channel for all observable EMRIs by spaceborne GW detectors and possibly a dominant channel for EMRIs hosted by MBHs heavier than a few $10^5 M_\odot$.

Throughout this Letter, we will use geometrical units $G = c = 1$ and assume a flat Λ CDM cosmology with $\Omega_m = 0.307$, $\Omega_\Lambda = 1 - \Omega_m$ and $H_0 = 67.7$ km/s/Mpc.

Disk-sBH interactions. In addition to the gravitational forces from the MBH and the stars/sBHs in the cluster, the orbital motion of a sBH around an accreting MBH is influenced by disk-sBH interactions: density waves, head wind [30–34] and other sub-dominant interactions including dynamic friction

[36, 37] and heating torque [38, 39].

As a sBH orbits around the MBH, its periodic motion excites density waves consisting of three components [32, 33]: regular density waves arising from the circular motion, eccentricity waves arising from the non-circular motion and bending waves arising from the motion normal to the disk. The density waves in turn affect the motion of the sBH: the regular density waves exert a (type-I) migration torque on the sBH and drives its migration in the radial direction on the timescale $t_{\text{mig,I}}$; the eccentricity and bending density waves damp the orbit eccentricity and the inclination with respect to the disk plane on the timescale t_{wav} . Previous analytic studies [32, 33] calibrated with numerical simulations [40] show that the type-I migration torque can be formulated as

$$j_{\text{mig,I}} = C_1 \frac{m_{\text{bh}}}{M} \frac{\Sigma}{M} \frac{r^4 \Omega^2}{h^2}, \quad (1)$$

where m_{bh} is sBH mass, and $M = M(< r)$ is the total mass of the MBH, stars and sBHs within radius r ; the prefactor $C_1 = -0.85 + d \log \Sigma / d \log r + 0.9 d \log T_{\text{mid}} / d \log r$ depends on the disk profile; $\Sigma(r)$, $T_{\text{mid}}(r)$, $h(r)$, $\Omega(r)$ are the disk surface density, the disk middle plane temperature, the disk aspect ratio and the sBH angular velocity, respectively. The corresponding migration timescale and damping timescale are

$$\begin{aligned} t_{\text{mig,I}} &= \frac{J}{|j_{\text{mig,I}}|} = \frac{r^2 \Omega}{|j_{\text{mig,I}}|} \sim \frac{M}{m_{\text{bh}}} \frac{M}{\Sigma r^2} \frac{h^2}{\Omega}, \\ t_{\text{wav}} &= \frac{M}{m_{\text{bh}}} \frac{M}{\Sigma r^2} \frac{h^4}{\Omega}, \end{aligned} \quad (2)$$

where $J = r^2 \Omega$ is the specific angular momentum of the sBH, and $t_{\text{wav}} \approx t_{\text{mig,I}} h^2$, i.e., the eccentricity/inclination damping is faster than the migration by a factor h^2 . A gap in the disk opens up if the sBH is so massive that its tidal torque removes surrounding gas faster than the gas replenishment via viscous diffusion. After a gap is opened, the type-I migration turns off and the sBH is subject to type-II migration driven by a type-II migration torque $j_{\text{mig,II}}$ [41].

For a sBH embedded in the gas disk, surrounding gas in its gravitational influence sphere flows towards it. Considering the differential rotation of the disk, the inflow gas generally carries nonzero angular momentum relative to the sBH, so that the inflow tends to circularize and form certain local disk or buldge profile around the sBH. Depending on the radiation feedback and magnetic fields, a major part of captured materials may escape in the form of outflow and only the remaining part is accreted by the sBH [42, 43]. Because of the circularization process, it is reasonable to expect that the outflow carries minimal net momentum with respect to the sBH. As a result, the head wind in the influence sphere of the sBH is captured, and the momentum carried by the wind eventually transfers to the sBH. Therefore the specific torque exerted on the sBH from the head wind is

$$j_{\text{wind}}^{\text{id}} = - \frac{r \delta v_{\phi} \dot{m}_{\text{gas}}}{m_{\text{bh}}}, \quad (3)$$

where the upper index ‘‘id’’ denotes in-disk objects, $\delta v_{\phi} := v_{\phi,\text{gas}} - v_{\phi,\text{bh}}$ is the head wind speed, and \dot{m}_{gas} is the amount of gas captured per unit time (see [12] for detailed calculation).

In summary, the migration timescales of in-disk (id) sBHs and those outside (od) are

$$t_{\text{mig}}^{\text{bh,id}} = \frac{J}{|j_{\text{mig,I,II}} + j_{\text{gw}} + j_{\text{wind}}|}, \quad t_{\text{mig}}^{\text{bh,od}} = \frac{J}{|j_{\text{mig,I}} + j_{\text{gw}}|}, \quad (4)$$

where $j_{\text{mig,I,II}} = j_{\text{mig,I}}$ or $j_{\text{mig,II}}$ and $j_{\text{wind}} = j_{\text{wind}}^{\text{id}}$ [Eq. (3)] or 0, depending on whether a gap is open. The specific torque arising from GW emissions is

$$j_{\text{gw}} = - \frac{32}{5} \frac{m_{\text{bh}}}{M} \left(\frac{M}{r} \right)^{7/2}. \quad (5)$$

The damping timescale of sBH orbital inclination and eccentricity is given by Eq. (2)

$$t_{\text{wav}}^{\text{bh,od}} = \frac{M}{m_{\text{bh}}} \frac{M}{\Sigma r^2} \frac{h^4}{\Omega}. \quad (6)$$

The above discussion of disk-sBH interactions also equally applies to stars in the cluster, except stars are usually lighter ($m_{\text{star}} < m_{\text{bh}}$), and the head wind impact on stars is weak ($j_{\text{wind}}^{\text{star}} \approx 0$) considering that the wind could be largely suppressed in the presence of star radiation feedback and solar wind [44, 45].

However, the structure of AGN disks has not been fully understood partially due to the large range over which an AGN disk extends: from an inner radius of a few gravitational radii of the MBH to the outer radius of parsec scale where the AGN disk connects to the galactic gas disk. Three commonly used AGN disk models: α -disk, β -disk [46] and TQM disk [47], are different in their prescriptions of disk viscosity and/or disk heating mechanism which lead to large differences in predicted disk structures. Each disk model is specified by two model parameters, the MBH accretion rate \dot{M}_{\bullet} and a viscosity parameter [12]: an α parameter which prescribes the ratio between the viscous stress and the local total/gas pressure in the α/β -disk and a X parameter which prescribes the ratio between the radial gas velocity and the local sound speed in the TQM disk.

Fokker-Planck equation. Statistical properties of stars and sBHs in the stellar cluster are encoded in their distribution functions $f_i(t, E, R)$ ($i = \text{star/bh}$) in the phase space, where

$$E := \phi(r) - v^2(r)/2, \quad R := J^2/J_c^2(E) \quad (7)$$

are the specific orbital (binding) energy and the normalized orbital angular momentum, respectively. Here $\phi(r)$ is the (positive) gravitational potential, v is the orbital speed, and $J_c(E)$ is the specific angular momentum of a circular orbiter with energy E . Given initial distributions $f_i(t = 0, E, R)$, the subsequent evolution is governed by the orbit-averaged Fokker-Planck equation. In the case of no gas disk, the Fokker-Planck equation (for both stars and sBHs) is formulated as [48–50]

$$C \frac{\partial f}{\partial t} = - \frac{\partial}{\partial E} F_E - \frac{\partial}{\partial R} F_R, \quad (8)$$

where $f = f_i(t, E, R)$, $C = C(E, R)$ is a normalization coefficient, and $F_{E,R}$ is the flux in the E/R direction:

$$\begin{aligned} -F_E &= \mathcal{D}_{EE} \frac{\partial f}{\partial E} + \mathcal{D}_{ER} \frac{\partial f}{\partial R} + \mathcal{D}_E f, \\ -F_R &= \mathcal{D}_{RR} \frac{\partial f}{\partial R} + \mathcal{D}_{ER} \frac{\partial f}{\partial E} + \mathcal{D}_R f, \end{aligned} \quad (9)$$

where the diffusion coefficients $\{\mathcal{D}_{EE}, \mathcal{D}_{ER}, \mathcal{D}_{RR}\}_i$ and the advection coefficients $\{\mathcal{D}_E, \mathcal{D}_R\}_i$ are functions of $f_i(t, E, R)$ [48–50]. From flux $\{F_E, F_R\}_{\text{bh}}$, we can compute the EMRI rate via the lose cone mechanism as

$$\Gamma_{\text{emri}}(t) = \int_{E > E_{\text{gw}}} \vec{F} \cdot d\vec{l}, \quad (10)$$

where $\vec{F} = (F_E, F_R)$, $d\vec{l} = (dE, dR)$ is the line element along the boundary of the loss cone, and E_{gw} is a characteristic energy scale above which the sBH GW emission is dominant with $t_{\text{gw}} < t_J$ [10–12, 23, 26].

In the presence of an AGN disk, stars and sBHs settle as two components: a cluster component and a disk component. We expect the distribution functions of cluster-component stars and sBHs acquire some dependence on the orbital inclination as interacting with the disk. For convenience, we choose to integrate out the inclination and work with the inclination-integrated distribution functions $f_i(t, E, R)$ of the cluster-component stars and sBHs. Considering the density waves excited on the disk to damp the orbital inclinations and eccentricities of orbiters, and to drive the orbiters' inward migration together with head winds and GW emissions, we rewrite the Fokker-Planck equation as

$$C \frac{\partial f}{\partial t} = -\frac{\partial}{\partial E} F_E - \frac{\partial}{\partial R} F_R + S, \quad (11)$$

where flux $F_{E,R}$ are defined in Eq. (9), with the advection coefficients modified by disk-star/sBH interactions as

$$\begin{aligned} \mathcal{D}_{E,\text{bh}} &\rightarrow \mathcal{D}_{E,\text{bh}} - C \frac{E}{t_{\text{mig}}^{\text{bh,od}}}, \\ \mathcal{D}_{R,\text{bh}} &\rightarrow \mathcal{D}_{R,\text{bh}} - C \frac{1-R}{t_{\text{wav}}^{\text{bh,od}}}, \\ \mathcal{D}_{E,\text{star}} &\rightarrow \mathcal{D}_{E,\text{star}} - C \frac{E}{t_{\text{mig}}^{\text{star,od}}}, \\ \mathcal{D}_{R,\text{star}} &\rightarrow \mathcal{D}_{R,\text{star}} - C \frac{1-R}{t_{\text{wav}}^{\text{star,od}}}, \end{aligned} \quad (12)$$

and the negative source term $S = S_i(t, E, R)$ arising from spherical-component stars/sBHs captured onto the disk is parameterized as

$$S_{\text{bh}} = -\mu_{\text{cap}} C \frac{f_{\text{bh}}}{t_{\text{mig}}^{\text{star,id}}}, \quad S_{\text{star}} = -\mu_{\text{cap}} \frac{m_{\text{star}}}{m_{\text{bh}}} C \frac{f_{\text{star}}}{t_{\text{mig}}^{\text{star,id}}}, \quad (13)$$

with $\mu_{\text{cap}} \in [h, 1] \frac{m_{\text{bh}}}{m_{\text{star}}}$ a phenomenological parameter quantifying the disk capture efficiency (see [12] for more details). A

new EMRI forms if a sBH is captured onto the disk and migrate to the vicinity of the MBH within the disk lifetime T_{disk} , therefore the wet EMRI rate is given by

$$\Gamma_{\text{emri}}(t; T_{\text{disk}}) = \int_{\substack{\text{bh, id} \\ \text{mig} < T_{\text{disk}}}} -S_{\text{bh}}(t, E, R) dE dR. \quad (14)$$

EMRI rate per MBH/AGN. Given initial distributions of stars and sBHs in the stellar cluster, one can evolve the system according to the Fokker-Planck equation (8) and calculate the EMRI rate in the loss cone channel using Eq. (10). As shown in Refs. [10–12], the EMRI rate mainly depends on the total number of stars within the MBH influence radius, which determines the relaxation timescale and the relative abundance of sBHs in the stellar cluster. Following Ref. [21], the time-averaged EMRI rate per MBH can be parameterized as

$$\tilde{\Gamma}_{\text{lc}}(M_{\bullet}; N_p) = C_{\text{dep}}(M_{\bullet}; N_p) C_{\text{grow}}(M_{\bullet}; N_p) \Gamma_{\text{lc}}(M_{\bullet}), \quad (15)$$

with

$$\Gamma_{\text{lc}}(M_{\bullet}) = 30 \left(\frac{M_{\bullet}}{10^6 M_{\odot}} \right)^{-0.19} \text{Gyr}^{-1}, \quad (16)$$

where N_p is the relative efficiency of prompt infalls over EMRIs; C_{dep} and C_{grow} are correction factors accounting for possible depletion of sBHs in the cusp as sBHs accreted by the MBH and capping the maximum MBH growth via accreting sBHs, respectively (see Supplemental Material [51] and Ref. [21] for calculation details) [52].

In Fig. 1, we show 3 sample models of dry EMRIs with $N_p = \{0, 10, 10^2\}$, where $\tilde{\Gamma}_{\text{lc}}(N_p = 0)$ is the same as the generic rate [Eq. (16)] in the mass range of interest, $\tilde{\Gamma}_{\text{lc}}(N_p = 10)$ is capped by the accretion growth limit C_{grow} in a low mass range, and $\tilde{\Gamma}_{\text{lc}}(N_p = 10^2)$ is further reduced by the sBH depletion C_{dep} across the entire mass range [51].

More technical complications are involved in calculating the AGN disk-assisted EMRI rate due to the uncertainties in AGN accretion. AGN accretion is likely episodic [53, 54], with the total duration of AGN accreting phases in the range of $10^7 - 10^9$ yrs according to Soltan's argument [55], therefore MBHs are in quiet phases in most time. Without detailed knowledge of the duty cycle of an MBH, we simplify it as a long quiet phase of $T_0 = 5$ Gyr followed by a short active phase of $T_{\text{disk}} = 10^7$ or 10^8 yr. Given initial distributions of stars and sBHs in the stellar cluster, we first evolve the system for time T_0 according to the Fokker-Planck equation (8), then turn on an accretion disk and continue the evolution for time T_{disk} , according to the modified Fokker-Planck equation (11). In the active phase, the disk assisted EMRI rate is computed using Eq. (14). We show the time-averaged EMRI rate per AGN

$$\tilde{\Gamma}_{\text{disk}}(M_{\bullet}; \mathbb{M}) = \frac{1}{T_{\text{disk}}} \int_{T_0}^{T_0 + T_{\text{disk}}} \Gamma_{\text{disk}}(t, M_{\bullet}; \mathbb{M}) dt, \quad (17)$$

for different models in Fig. 1, where \mathbb{M} denotes models with parameters as initial distributions of stars and sBHs in the

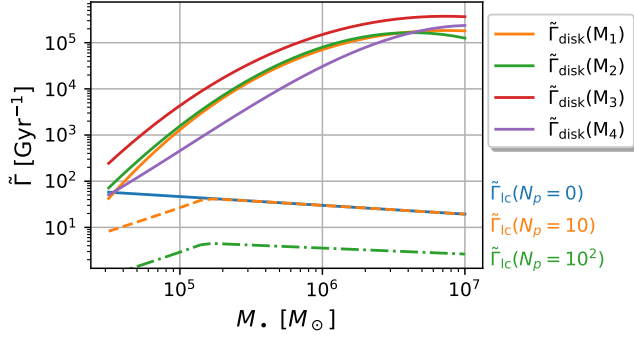


FIG. 1. Average EMRI rates per MBH in the loss cone channel $\tilde{\Gamma}_{\text{lc}}(M_{\bullet}; N_p)$ and per AGN in the AGN disk channel $\tilde{\Gamma}_{\text{disk}}(M_{\bullet}; \mathbb{M})$, where N_p is the relative efficiency of prompt infalls over EMRIs; \mathbb{M} consists of all model parameters of initial condition of stellar clusters, AGN duty cycles and AGN disk model. In the plot, we show 3 sample models of dry EMRIs with $N_p = \{0, 10, 10^2\}$ and 4 sample models of wet EMRIs with $\mathbb{M} = \mathbb{M}_{1,\dots,4}$.

cluster, duty cycles of MBHs and AGN disk model (see Supplemental Material [51] for model details). Because sBHs are captured onto the disk and migrate inward efficiently, the wet EMRI formation rate is mainly limited by the number of sBHs available in the stellar cluster. As a result, the average wet EMRI rates are higher for heavier MBH hosts, where more sBHs are available.

In Fig. 1, we show the wet EMRI rate per AGN for 4 example models \mathbb{M} . It is evident that the presence of an AGN disk boosts the EMRI formation rate by orders of magnitude [12, 56], and the amplification is stronger for heavier MBHs.

Total and LISA detectable EMRI rates. For calculating the total EMRI rate, we consider two redshift-independent MBH mass functions in the range of $(10^4, 10^7)M_{\odot}$,

$$f_{\bullet,-0.3} : \frac{dN_{\bullet}}{d \log M_{\bullet}} = 0.01 \left(\frac{M_{\bullet}}{3 \times 10^6 M_{\odot}} \right)^{-0.3} \text{ Mpc}^{-3}, \quad (18)$$

$$f_{\bullet,+0.3} : \frac{dN_{\bullet}}{d \log M_{\bullet}} = 0.002 \left(\frac{M_{\bullet}}{3 \times 10^6 M_{\odot}} \right)^{+0.3} \text{ Mpc}^{-3},$$

where the former one is approximate to the mass function as modelled in Refs. [57–60] assuming MBHs were seeded by Population III stars and accumulated mass via mergers and gas accretion along cosmic history, and the latter one is a phenomenological model [17]. The differential EMRI rates (in observer’s frame) in the two formation channels are written as

$$\frac{d^2 \mathcal{R}_{\text{lc}}}{dM_{\bullet} dz} = \frac{1}{1+z} \frac{dN_{\bullet}}{d \log M_{\bullet}} \frac{dV_c(z)}{dz} C_{\text{cusp}}(M_{\bullet}, z) \tilde{\Gamma}_{\text{lc}}(M_{\bullet}; N_p), \quad (19)$$

$$\frac{d^2 \mathcal{R}_{\text{disk}}}{dM_{\bullet} dz} = \frac{f_{\text{AGN}}}{1+z} \frac{dN_{\bullet}}{d \log M_{\bullet}} \frac{dV_c(z)}{dz} C_{\text{cusp}}(M_{\bullet}, z) \tilde{\Gamma}_{\text{disk}}(M_{\bullet}; \mathbb{M}),$$

where the factor $1/(1+z)$ arises from the cosmological redshift, $V_c(z)$ is the comoving volume of the universe up to redshift z , $C_{\text{cusp}}(M_{\bullet}, z)$ is the fraction of MBHs living in stellar

cusps which are supposed to be evacuated during mergers of binary MBHs and re-grow afterwards [57–60]. For cases with mass function $f_{\bullet,+0.3}$, we use the same C_{cusp} function as in [21] and we simply take $C_{\text{cusp}} = 1$ for cases with phenomenological mass function $f_{\bullet,+0.3}$ [61]. We conservatively assume a constant AGN fraction $f_{\text{AGN}} = 1\%$ throughout the universe, though it can be 10 times higher [28, 29].

In order to calculate the LISA detectable EMRI rate in each channel, we construct a population of EMRIs with sBH mass $m_{\text{bh}} = 10M_{\odot}$, MBH spin $a = 0.98$, and MBH masses and redshifts randomly sampled according to the differential EMRI rates [Eq. (19)]. For each individual EMRI, we need 10 more parameters to uniquely specify its binary configuration at coalescence and its gravitational waveform [62–64]: sky localization \hat{n} , MBH spin direction \hat{a} , 3 phase angles, coalescence time t_0 , inclination angle ι_0 and eccentricity e_0 at coalescence. For EMRIs of both formation channels, we assume the sky locations and the MBH spin directions are isotropically distributed on the sphere, 3 phase angles are uniformly distributed in $[0, 2\pi]$, coalescence times are randomly sampled from $[0, 2]$ yr, and cosines of inclination angles are randomly sampled from $[-1, 1]$. Distributions of eccentricity e_0 are different for the two channels: uniform distribution of e_0 in $[0, 0.2]$ for the loss cone channel v.s. $e_0 = 0$ for the AGN disk channel.

For each EMRI, we compute its time-domain waveform $h_{+,\times}(t)$ using the Augment Analytic Kludge (AAK) [62–64] with the conservative Schwarzschild plunge condition, because the PN corrections used for constructing the AAK waveform model are increasingly inaccurate as the orbital separation decreases. Extending the waveform to the Kerr last stable orbit likely leads to an overestimate of the signal-to-noise ratio (SNR) [21, 64]. The SNR is calculated as a noise weighted inner product in the frequency domain

$$\text{SNR} = \sqrt{4 \int_0^{\infty} \frac{h_+(f)h_+^*(f) + h_{\times}(f)h_{\times}^*(f)}{S_n(f)} df}, \quad (20)$$

where $S_n(f)$ is the sky-averaged detector sensitivity of LISA [21, 65]. The expected LISA detectable EMRI rates ($\text{SNR} \geq 20$) of different models in each mass bin are shown in Fig. 2 (see Supplemental Material [51] for the total event rates and the LISA detectable rates). From Fig. 2, EMRI formation in AGN disks is evidently an important channel, and is a dominant channel for EMRIs hosted by heavy MBHs ($M_{\bullet} \gtrsim$ a few $10^5 M_{\odot}$) for all the models we have considered.

Applications of wet EMRIs. Wet EMRIs may be distinguished from dry EMRIs from eccentricity measurements, as wet EMRIs are circular because of disk interactions and dry EMRIs are generally eccentric. Similar to dry EMRIs, MBH masses, spins, correlation of the MBH spin direction and the rotation direction of galactic gas disk, and luminosity distances extracted from wet EMRIs (with a possibly higher event rate) can be used to constrain the growth history of MBHs [16–18] and the low-redshift cosmology [19]. Wet EMRIs encode additional information of MBH growth in their

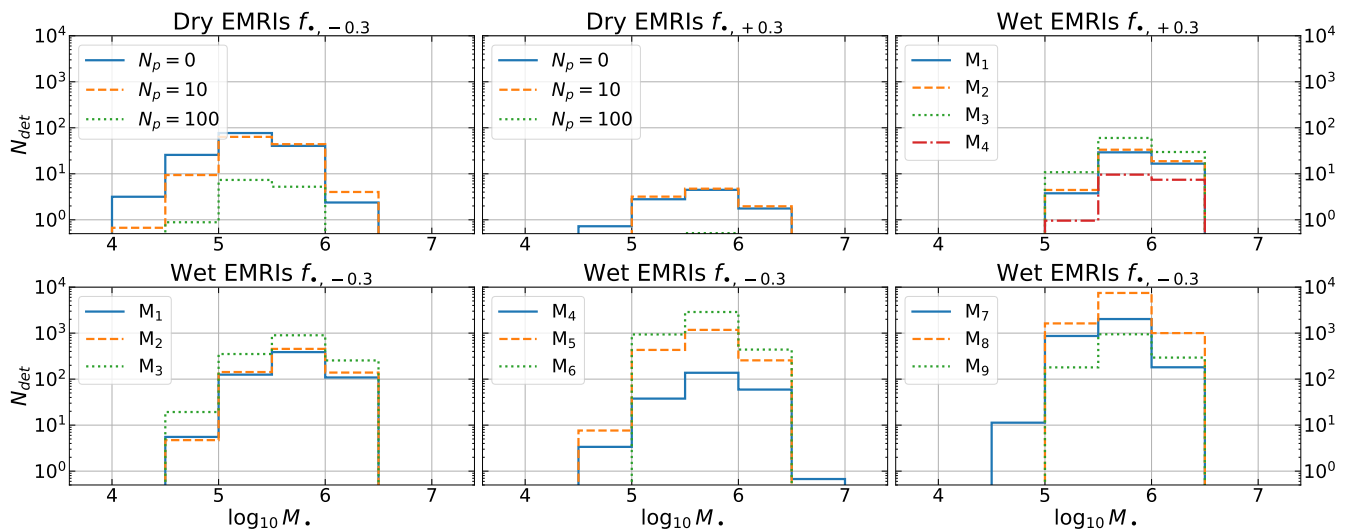


FIG. 2. Forecasted LISA detectable dry and wet EMRI rates N_{det} per mass bin ($M_* [M_\odot]$) per year for different models, where $f_{*, \pm 0.3}$ are the two different MBH mass functions [Eq. (18)], N_p is the relative efficiency of prompt infalls over EMRIs in the loss cone channel, and the wet EMRI model parameters of $M_{1, \dots, 9}$ are detailed in Supplemental Material [51].

orbital inclination angles ι_0 . If all MBHs grow up via coherent gas accretion where gas feeds are from a fixed direction, orbital inclination angles of wet EMRIs at coalescence should be $\iota_0 \approx \pi/2$. If MBHs grow up via chaotic gas accretion from a random direction in each active phase, a fraction of wet EMRIs form before the MBH spin direction \hat{a} is aligned with the disk rotation direction \hat{L} via the Bardeen-Petterson mechanism [66], and their orbital inclinations are approximately $i_0 \approx \cos^{-1}(\hat{a} \cdot \hat{L})$. In a similar way, MBH growth via different merger channels also imprints different signatures on the inclination angles of wet EMRIs.

Combining GW observations of wet EMRIs by spaceborne detectors with radio observations of AGN jets by, e.g., next-generation Event Horizon Telescope (ngEHT) [67], one can simultaneously measure the MBH mass M_* , the MBH spin \hat{a} , the rotation direction of the accretion disk \hat{L} , the jet power \dot{E}_{jet} and the jet direction \hat{n}_{jet} . This set of observables provide unprecedented opportunities to probe the AGN jet physics. For example, an ensemble of events with $\{\hat{n}_{\text{jet}} \cdot \hat{a}, \hat{n}_{\text{jet}} \cdot \hat{L}\}$ data may help us to constrain various jet launching models, i.e., powered by the rotating energy of the MBH [68] or by the accretion disk [69]. In addition, the disk environmental effects may induce measurable phase shifts to the gravitational waveforms of wet EMRIs [34, 70], therefore certain disk properties are directly constrained with GW observations. AGN disk properties are also one of the primary targets of ngEHT, which makes accretion physics another realm where LISA and ngEHT may synergize.

We thank Hui-Min Fan and Alberto Sesana for very helpful discussions. The authors are supported by the Natural Sciences and Engineering Research Council of Canada and in part by Perimeter Institute for Theoretical Physics. Research

at Perimeter Institute is supported in part by the Government of Canada through the Department of Innovation, Science and Economic Development Canada and by the Province of Ontario through the Ministry of Colleges and Universities.

* zpan@perimeterinstitute.ca

† hyang@perimeterinstitute.ca

- [1] J. Baker, J. Bellovary, P. L. Bender, E. Berti, R. Caldwell, J. Camp, J. W. Conklin, N. Cornish, C. Cutler, R. DeRosa, M. Eracleous, E. C. Ferrara, S. Francis, M. Hewitson, K. Holley-Bockelmann, A. Hornschemeier, C. Hogan, B. Kamaï, B. J. Kelly, J. Shapiro Key, S. L. Larson, J. Livas, S. Manthripragada, K. McKenzie, S. T. McWilliams, G. Mueller, P. Natarajan, K. Numata, N. Rioux, S. R. Sankar, J. Schnittman, D. Shoemaker, D. Shoemaker, J. Slutsky, R. Spero, R. Stebbins, I. Thorpe, M. Vallisneri, B. Ware, P. Wass, A. Yu, and J. Ziemer, arXiv e-prints , arXiv:1907.06482 (2019), [arXiv:1907.06482](https://arxiv.org/abs/1907.06482) [astro-ph.IM].
- [2] J. Mei, Y.-Z. Bai, J. Bao, E. Barausse, and et al., *Progress of Theoretical and Experimental Physics* (2020), [10.1093/ptep/ptaa114](https://arxiv.org/abs/10.1093/ptep/ptaa114).
- [3] M. Arca-Sedda and R. Capuzzo-Dolcetta, *MNRAS* **483**, 152 (2019), [arXiv:1709.05567](https://arxiv.org/abs/1709.05567) [astro-ph.GA].
- [4] M. Arca-Sedda, P. Amaro-Seoane, and X. Chen, arXiv e-prints , arXiv:2007.13746 (2020), [arXiv:2007.13746](https://arxiv.org/abs/2007.13746) [astro-ph.GA].
- [5] P. Amaro-Seoane, *Phys. Rev. D* **99**, 123025 (2019), [arXiv:1903.10871](https://arxiv.org/abs/1903.10871) [astro-ph.GA].
- [6] P. Amaro-Seoane, arXiv e-prints , arXiv:2011.03059 (2020), [arXiv:2011.03059](https://arxiv.org/abs/2011.03059) [gr-qc].
- [7] Z. Khakhaleva-Li and C. J. Hogan, arXiv e-prints , arXiv:2006.00438 (2020), [arXiv:2006.00438](https://arxiv.org/abs/2006.00438) [astro-ph.CO].
- [8] K. Glampedakis and S. Babak, *Classical and Quantum Gravity* **23**, 4167 (2006), [arXiv:gr-qc/0510057](https://arxiv.org/abs/gr-qc/0510057) [gr-qc].
- [9] L. Barack and C. Cutler, *Phys. Rev. D* **75**, 042003 (2007),

- arXiv:gr-qc/0612029 [gr-qc].
- [10] M. Preto and P. Amaro-Seoane, *Astrophys.J.Lett.* **708**, L42 (2010), arXiv:0910.3206 [astro-ph.GA].
- [11] P. Amaro-Seoane and M. Preto, *Classical and Quantum Gravity* **28**, 094017 (2011), arXiv:1010.5781 [astro-ph.CO].
- [12] Z. Pan and H. Yang, (2021), arXiv:2101.09146 [astro-ph.HE].
- [13] B. Bonga, H. Yang, and S. A. Hughes, *Phys. Rev. Lett.* **123**, 101103 (2019), arXiv:1905.00030 [gr-qc].
- [14] H. Yang, B. Bonga, Z. Peng, and G. Li, *Phys. Rev. D* **100**, 124056 (2019), arXiv:1910.07337 [gr-qc].
- [15] E. Barausse, V. Cardoso, and P. Pani, *Phys. Rev. D* **89**, 104059 (2014), arXiv:1404.7149 [gr-qc].
- [16] E. Berti and M. Volonteri, *Astrophys. J.* **684**, 822 (2008), arXiv:0802.0025 [astro-ph].
- [17] J. R. Gair, C. Tang, and M. Volonteri, *Phys. Rev. D* **81**, 104014 (2010), arXiv:1004.1921 [astro-ph.GA].
- [18] Z. Pan and H. Yang, *Astrophys. J.* **901**, 163 (2020), arXiv:2007.03783 [astro-ph.CO].
- [19] D. Laghi, N. Tamanini, W. Del Pozzo, A. Sesana, J. Gair, and S. Babak, arXiv e-prints, arXiv:2102.01708 (2021), arXiv:2102.01708 [astro-ph.CO].
- [20] P. Amaro-Seoane, *Living Reviews in Relativity* **21**, 4 (2018), arXiv:1205.5240 [astro-ph.CO].
- [21] S. Babak, J. Gair, A. Sesana, E. Barausse, C. F. Sopuerta, C. P. L. Berry, E. Berti, P. Amaro-Seoane, A. Petiteau, and A. Klein, *Phys. Rev. D* **95**, 103012 (2017), arXiv:1703.09722 [gr-qc].
- [22] J. R. Gair, S. Babak, A. Sesana, P. Amaro-Seoane, E. Barausse, C. P. Berry, E. Berti, and C. Sopuerta, *J. Phys. Conf. Ser.* **840**, 012021 (2017), arXiv:1704.00009 [astro-ph.GA].
- [23] C. Hopman and T. Alexander, *Astrophys. J.* **629**, 362 (2005), arXiv:astro-ph/0503672 [astro-ph].
- [24] B. Bar-Or and T. Alexander, *Astrophys. J.* **820**, 129 (2016), arXiv:1508.01390 [astro-ph.GA].
- [25] H.-M. Fan, Y.-M. Hu, E. Barausse, A. Sesana, J.-d. Zhang, X. Zhang, T.-G. Zi, and J. Mei, *Phys. Rev. D* **102**, 063016 (2020), arXiv:2005.08212 [astro-ph.HE].
- [26] L. Zwick, P. R. Capelo, E. Bortolas, V. Vazquez-Aceves, L. Mayer, and P. Amaro-Seoane, arXiv e-prints, arXiv:2102.00015 (2021), arXiv:2102.00015 [astro-ph.GA].
- [27] P. C. Peters and J. Mathews, *Physical Review* **131**, 435 (1963).
- [28] A. Galametz, D. Stern, P. R. M. Eisenhardt, M. Brodwin, M. J. I. Brown, A. Dey, A. H. Gonzalez, B. T. Jannuzi, L. A. Moustakas, and S. A. Stanford, *Astrophys. J.* **694**, 1309 (2009), arXiv:0901.1109 [astro-ph.CO].
- [29] M. Macuga, P. Martini, E. D. Miller, M. Brodwin, M. Hayashi, T. Kodama, Y. Koyama, R. A. Overzier, R. Shimakawa, K.-i. Tadaki, and I. Tanaka, *Astrophys. J.* **874**, 54 (2019), arXiv:1805.06569 [astro-ph.GA].
- [30] P. Goldreich and S. Tremaine, *Astrophys. J.* **233**, 857 (1979).
- [31] P. Goldreich and S. Tremaine, *Astrophys. J.* **241**, 425 (1980).
- [32] H. Tanaka, T. Takeuchi, and W. R. Ward, *Astrophys. J.* **565**, 1257 (2002).
- [33] H. Tanaka and W. R. Ward, *Astrophys. J.* **602**, 388 (2004).
- [34] B. Kocsis, N. Yunes, and A. Loeb, *Phys. Rev. D* **84**, 024032 (2011), arXiv:1104.2322 [astro-ph.GA].
- [35] More details can be found in a companion paper [12].
- [36] S. Chandrasekhar, *Astrophys. J.* **97**, 255 (1943).
- [37] E. C. Ostriker, *Astrophys. J.* **513**, 252 (1999), arXiv:astro-ph/9810324 [astro-ph].
- [38] F. S. Masset, *MNRAS* **472**, 4204 (2017), arXiv:1708.09807 [astro-ph.EP].
- [39] A. M. Hankla, Y.-F. Jiang, and P. J. Armitage, *Astrophys. J.* **902**, 50 (2020), arXiv:2005.03785 [astro-ph.EP].
- [40] S. J. Paardekooper, C. Baruteau, A. Crida, and W. Kley, *MNRAS* **401**, 1950 (2010), arXiv:0909.4552 [astro-ph.EP].
- [41] D. Syer and C. J. Clarke, *MNRAS* **277**, 758 (1995), arXiv:astro-ph/9505021 [astro-ph].
- [42] X.-H. Yang, F. Yuan, K. Ohsuga, and D.-F. Bu, *Astrophys. J.* **780**, 79 (2014), arXiv:1306.1871 [astro-ph.HE].
- [43] J. C. McKinney, A. Tchekhovskoy, A. Sadowski, and R. Narayan, *MNRAS* **441**, 3177 (2014), arXiv:1312.6127 [astro-ph.CO].
- [44] A. Gruzinov, Y. Levin, and C. D. Matzner, *MNRAS* **492**, 2755 (2020), arXiv:1906.01186 [astro-ph.HE].
- [45] X. Li, P. Chang, Y. Levin, C. D. Matzner, and P. J. Armitage, *MNRAS* **494**, 2327 (2020), arXiv:1912.06864 [astro-ph.HE].
- [46] E. Sirko and J. Goodman, *MNRAS* **341**, 501 (2003), arXiv:astro-ph/0209469 [astro-ph].
- [47] T. A. Thompson, E. Quataert, and N. Murray, *Astrophys. J.* **630**, 167 (2005), arXiv:astro-ph/0503027 [astro-ph].
- [48] H. Cohn and R. M. Kulsrud, *Astrophys. J.* **226**, 1087 (1978).
- [49] H. Cohn, *Astrophys. J.* **234**, 1036 (1979).
- [50] J. Binney and S. Tremaine, *Galactic dynamics* (1987).
- [51] “See Supplemental Material at [] for more details of the average EMRI rates, and the total event rates and LISA detectable rates for different models.”
- [52] The loss-cone EMRI rate in Eq. (16) is lower than previous calculations [10–12, 21] by one order of magnitude because these previous results were based on the Peters’ formula [27] which underestimate the GW emission timescales of eccentric binaries and the true EMRI rate should be lower by at least one order of magnitude as pointed out in [26].
- [53] A. King and C. Nixon, *MNRAS* **453**, L46 (2015), arXiv:1507.05960 [astro-ph.HE].
- [54] K. Schawinski, M. Koss, S. Berney, and L. F. Sartori, *MNRAS* **451**, 2517 (2015), arXiv:1505.06733 [astro-ph.GA].
- [55] A. Soltan, *MNRAS* **200**, 115 (1982).
- [56] H. Tagawa, Z. Haiman, and B. Kocsis, *Astrophys. J.* **898**, 25 (2020), arXiv:1912.08218 [astro-ph.GA].
- [57] E. Barausse, *MNRAS* **423**, 2533 (2012), arXiv:1201.5888 [astro-ph.CO].
- [58] A. Sesana, E. Barausse, M. Dotti, and E. M. Rossi, *Astrophys. J.* **794**, 104 (2014), arXiv:1402.7088 [astro-ph.CO].
- [59] F. Antonini, E. Barausse, and J. Silk, *Astrophys.J.Lett.* **806**, L8 (2015), arXiv:1504.04033 [astro-ph.GA].
- [60] F. Antonini, E. Barausse, and J. Silk, *Astrophys. J.* **812**, 72 (2015), arXiv:1506.02050 [astro-ph.GA].
- [61] There was some misplot of the $C_{\text{cusp}}(M_{\bullet}, z)$ function in [21], and we thank Alberto Sesana for kindly providing the correct one.
- [62] L. Barack and C. Cutler, *Phys. Rev. D* **69**, 082005 (2004), arXiv:gr-qc/0310125.
- [63] A. J. Chua and J. R. Gair, *Class. Quant. Grav.* **32**, 232002 (2015), arXiv:1510.06245 [gr-qc].
- [64] A. J. Chua, C. J. Moore, and J. R. Gair, *Phys. Rev. D* **96**, 044005 (2017), arXiv:1705.04259 [gr-qc].
- [65] P. Amaro-Seoane, H. Audley, S. Babak, and et al., arXiv e-prints, arXiv:1702.00786 (2017), arXiv:1702.00786 [astro-ph.IM].
- [66] J. M. Bardeen and J. A. Petterson, *Astrophys.J.Lett.* **195**, L65 (1975).
- [67] <https://www.ngeht.org/>.
- [68] R. D. Blandford and R. L. Znajek, *MNRAS* **179**, 433 (1977).
- [69] R. D. Blandford and D. G. Payne, *Mon. Not. Roy. Astron. Soc.* **199**, 883 (1982).
- [70] E. Barausse, V. Cardoso, and P. Pani, *Phys. Rev. D* **89**, 104059 (2014), arXiv:1404.7149 [gr-qc].
- [71] K. Gültekin, D. O. Richstone, K. Gebhardt, T. R. Lauer,

S. Tremaine, M. C. Aller, R. Bender, A. Dressler, S. M. Faber, A. V. Filippenko, R. Green, L. C. Ho, J. Kormendy, J. Magorrian, J. Pinkney, and C. Siopis, *Astrophys. J.* **698**, 198 (2009), arXiv:0903.4897 [astro-ph.GA].

Supplemental Material

Following Ref. [21], we explain the two corrections $C_{\text{dep}}(M_\bullet; N_p)$ and $C_{\text{grow}}(M_\bullet; N_p)$ to the generic dry EMRI rate. Consider a MBH with mass M_\bullet , whose influence sphere ($r < r_c = 2M_\bullet/\sigma^2$) encloses a number of sBHs with total mass $\Sigma m_{\text{bh}} \simeq 0.06M_\bullet$, and these sBHs will be depleted by the MBH via EMRIs and prompt infalls on a timescale

$$\begin{aligned} T_{\text{dep}}(r_c) &= \frac{\Sigma m_{\text{bh}}}{(1 + N_p)\Gamma_{\text{lc}}(M_\bullet)m_{\text{bh}}} \\ &= \frac{200}{1 + N_p} \left(\frac{m_{\text{bh}}}{10M_\odot}\right)^{-1} \left(\frac{M_\bullet}{10^6M_\odot}\right)^{1.19}, \end{aligned} \quad (21)$$

where N_p is the relative efficiency of prompt infalls over EMRIs. On the influence sphere, the relaxation timescale of the star cluster is approximately [50]

$$T_{\text{rlx}}(r_c) \simeq \left(\frac{\sigma}{20\text{km/s}}\right) \left(\frac{r_c}{1\text{pc}}\right)^2, \quad (22)$$

where the velocity dispersion is related to the MBH mass by the famous $M_\bullet - \sigma$ relation [71]. The depletion correction C_{dep} is defined as

$$C_{\text{dep}}(M_\bullet; N_p) := \min\left\{\frac{T_{\text{dep}}}{T_{\text{rlx}}}, 1\right\}, \quad (23)$$

where

$$\frac{T_{\text{dep}}}{T_{\text{rlx}}} \simeq \frac{12}{1 + N_p} \left(\frac{m_{\text{bh}}}{10M_\odot}\right)^{-1} \left(\frac{M_\bullet}{10^6M_\odot}\right)^{0.06}. \quad (24)$$

The growth correction

$$C_{\text{grow}} := \min\left\{e^{-1} \frac{M_\bullet}{\Delta M_\bullet}, 1\right\} \quad (25)$$

arises from requiring the MBH grows no more than e^{-1} via accreting sBHs, where

$$\Delta M_\bullet = m(1 + N_p)C_{\text{dep}}(M_\bullet; N_p)\Gamma_{\text{lc}}(M_\bullet)T_{\text{emri}}(M_\bullet), \quad (26)$$

is the MBH growth via accreting sBHs, and

$$T_{\text{emri}}(M_\bullet) = \int dz \frac{dt}{dz} C_{\text{cusp}}(M_\bullet, z) \quad (27)$$

is the effective growth time when the MBH lives in a stellar cusp. As show in Fig. 1 in the main text, the growth correction C_{grow} only makes a difference for MBHs $\lesssim 10^5 M_\odot$, and C_{grow} only makes a difference for $N_p \gtrsim 10$.

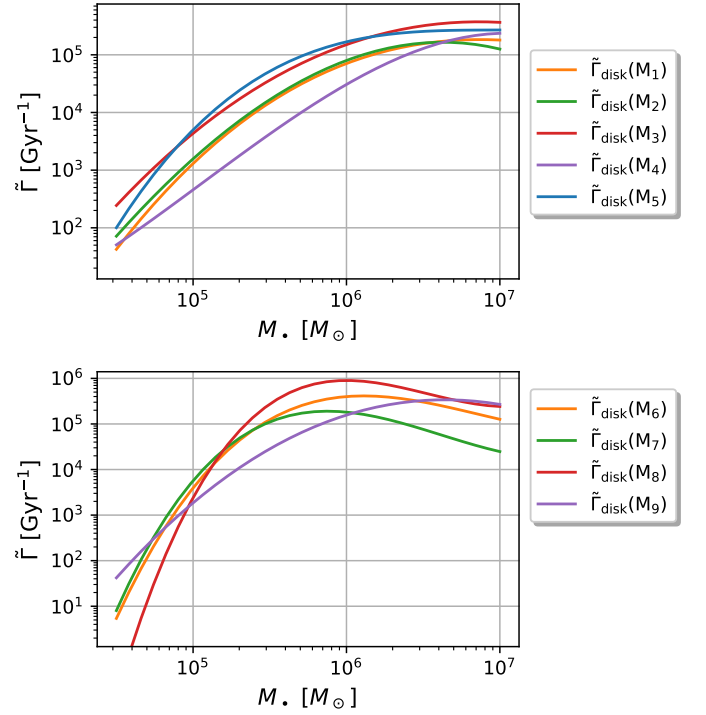


FIG. 3. Average wet EMRI rates per AGN $\tilde{\Gamma}_{\text{disk}}(M_\bullet; M)$ for all the 9 different models we considered.

For calculating the wet EMRI rate, we need to specify the initial distributions of stars and sBHs in the stellar cluster, the AGN duty cycle and the AGN disk structure (see [12] for more details). For the initial condition of the stellar cluster, we assume the Tremaine's cluster model with a power-law density profile $n_{\text{star}}(r) \sim r^{-\gamma}$ deep inside the influence sphere of the MBH and $n_{\text{star}}(r) \sim r^{-4}$ far outside, and sBHs are of the same density profile with a relative abundance δ . Without detailed knowledge of the AGN duty cycle, we simplify it as a long quiet phase with duration $T_0 = 5$ Gyr followed by a short active phase with duration T_{disk} . As the structure of AGN disks is subject to large uncertainties, we consider both an α -disk model [46] with the viscosity parameter $\alpha = 0.1$ and accretion rate $\dot{M}_\bullet = 0.1\dot{M}_\bullet^{\text{Edd}}$, and a TQM disk [47] with the viscosity parameter $X = 0.1$ and accretion rate $\dot{M}_\bullet = 0.1\dot{M}_\bullet^{\text{Edd}}$ (β -disk is different from α -disk only in the inner region where radiation pressure dominates over gas pressure, and this difference has little impact on the wet EMRI rate). As shown in the companion paper [12], the efficiency of sBHs captured into the disk is not completely clear, and we choose to quantify the uncertainty with a free parameter μ_{cap} [Eq. (13) in the main text]. In this work, we consider 9 representative models whose model parameters are compiled in Table I, and their average wet EMRI rates per AGN are shown in Fig. 3.

In Table I, we summarize the total EMRI rates and the LISA detectable rates from each formation channel for all the different models we have considered.

TABLE I. Comparison of dry and wet EMRI rates in different models, where f_{\bullet} is the MBH mass function. The last two columns are the total EMRI rate in the redshift range of $0 < z < 4.5$ and the corresponding LISA detectable ($\text{SNR} \geq 20$) rate.

		f_{\bullet}	N_p				Total rate [yr^{-1}]	LISA detectable rate [yr^{-1}]	
Dry EMRIs			0				3500	150	
		$f_{\bullet,-0.3}$	10				1300	120	
			10^2				150	14	
		$f_{\bullet,+0.3}$	0				160	10	
			10				130	10	
			10^2				15	1	
		f_{\bullet}	$\mathbb{M} : (\gamma, \delta)$	μ_{cap}	T_{disk} [yr]	AGN Disk	Total rate [yr^{-1}]	LISA detectable rate [yr^{-1}]	
Wet EMRIs		$f_{\bullet,-0.3}$	$M_1 :$	(1.5, 0.001)	1			11000	600
			$M_2 :$	(1.5, 0.001)	0.1	10^8	α -disk	11000	760
			$M_3 :$	(1.5, 0.002)	1			24000	1500
			$M_4 :$	(1.8, 0.001)	1			8100	240
		$f_{\bullet,+0.3}$	$M_5 :$	(1.5, 0.001)	1	10^8	TQM disk	23000	1900
			$M_6 :$	(1.5, 0.001)	1			39000	4200
			$M_7 :$	(1.5, 0.001)	0.1	10^7	α -disk	21000	3000
			$M_8 :$	(1.5, 0.002)	1			80000	9800
			$M_9 :$	(1.8, 0.001)	1			22000	1400
		$f_{\bullet,+0.3}$	$M_1 :$	(1.5, 0.001)	1			2100	49
			$M_2 :$	(1.5, 0.001)	0.1	10^8	α -disk	2000	57
			$M_3 :$	(1.5, 0.002)	1			4300	100
			$M_4 :$	(1.8, 0.001)	1			1900	18